Nanoscale

PAPER

View Article Online
View Journal | View Issue

Cite this: *Nanoscale*, 2024, **16**, 9426

Strategic design of VO_2 encased in N-doped carbon as an efficient electrocatalyst for the nitrogen reduction reaction in neutral and acidic media†

Ashis Chhetri,‡[a,b] Ashmita Biswas, ‡[c] Sumana Podder,[a,b] Ramendra Sundar Dey *[c] and Joyee Mitra *[a,b]

Electrocatalytic nitrogen fixation to ammonia (NH_3), a precursor for fertilizer production and a promising energy carrier, has garnered widespread interest as an environment-friendly and sustainable alternative to the energy-intensive fossil-feedstock-dependent Haber–Bosch process. The large-scale deployment of this process is contingent on the identification of inexpensive, Earth-abundant systems that can operate efficiently, irrespective of the electrolyte pH for the selective production of NH_3. In this regard, we discuss the scalable synthesis of VO_2 anchored on N-doped carbon (**VO_2@CN**), and its applicability as a robust electrocatalyst for the nitrogen reduction reaction (NRR). Benefitting from the presence of exposed VO_2, which presumably acts as the active site for nitrogen reduction, and its activity over a broad pH range (from acidic to neutral), **VO_2@CN** exhibits a high NH_3 yield of 0.31 and 0.52 μmol h^{-1} mg_{cat}^{-1} and a maximum Faradaic efficiency (FE) of 67.9% and 61.9% at −0.1 V *vs*. RHE, under neutral and acidic conditions, respectively. The obscured reaction intermediates of the NRR were identified from *in situ* ATR-IR studies under both electrolyte conditions. Additionally, the high selectivity of the catalyst was ascertained from the absence of hydrazine production and the competing hydrogen evolution reaction (HER). However, ammonia production underwent a reduction over 12 h of continuous operation presumably owing to the leaching of catalyst under these electrolysis conditions, which was more pronounced in electrolytes with acidic pH. Overall, the present report unveils the performance of an earth-abundant vanadium oxide-based system as an efficient electrocatalyst for the NRR under acidic and neutral pH conditions.

Received 14th February 2024,
Accepted 22nd March 2024

DOI: 10.1039/d4nr00640b

rsc.li/nanoscale

Introduction

Ammonia (NH_3) obtained from the reduction of nitrogen is perceived as a clean energy carrier and a replacement for gaseous hydrogen owing to its compression to the liquid state at a low pressure of ∼8 bar and room temperature and its high energy density in the liquid state.[1,2] In addition, NH_3 is vital in agriculture, in the production of fertilizers to feed the ever-increasing global population. The industrial production of NH_3 relies on the Haber–Bosch process, which requires harsh temperature (400–600 °C) and pressure (20–40 MPa) conditions, has an energy efficiency of ∼65%, and accounts for about 2% of global energy consumption, releasing a large amount of CO_2 into the atmosphere causing an increase in the global temperature.[3–5] This emphasizes the necessity of developing a clean, sustainable alternative process for nitrogen fixation, which precludes the necessity of elevated temperatures and reduces the carbon footprint.[6,7] Various routes for nitrogen fixation, including photochemical, electrochemical and biological approaches have been explored by the research community to arrive at environmentally safe and energy-efficient methods to artificially fix nitrogen.[8–11] Among these approaches, the electrochemical NRR is considered a promising alternative to NH_3 production due to its mild reaction conditions and environmentally friendly precursors of N_2 and H_2O, which can revolutionize green ammonia production when used in conjunction with renewable energy resources.[5,12] Intensive efforts have been devoted worldwide to the design

[a]*Inorganic Materials and Catalysis Division, CSIR-Central Salt and Marine Chemicals Research Institute, Gijubhai Badheka Marg, Bhavnagar 364002, Gujarat, India. E-mail: joyeemitra@csmcri.res.in, joyeemitra@gmail.com*
[b]*Academy of Scientific and Innovative Research (AcSIR), Ghaziabad 201002, India*
[c]*Institute of Nano Science and Technology, Sector 81, Mohali 140306, Punjab, India. E-mail: rsdey@inst.ac.in*

†Electronic supplementary information (ESI) available. See DOI: https://doi.org/10.1039/d4nr00640b

‡These authors contributed equally to this work.

and investigation of catalysts for the selective production of NH_3 *via* the NRR with a high FE.[13–19] It is extremely arduous to dissociate the inert dinitrogen molecule (bond energy of N_2 is 941 kJ mol^{-1}), and mechanistically, the NRR involves multiple proton-coupled electron-transfer steps.[20] In addition, the utility of the process is limited by the competing hydrogen evolution reaction (HER), which has faster kinetics and operates under a similar potential window.

The literature reveals a series of transition metal-based systems that have been reported to facilitate the NRR under ambient conditions.[21–28] Of these, Mo, Fe, Rh and Ru are at the top of the volcano diagram, and hence, they show the best activity.[23] However, the competing HER lowers their efficiency for ammonia production. Early transition metals including Zr, Ti, Sc, V *etc*., have been reported to bind N-adatoms more strongly compared to H-adatoms, thereby enhancing the production of NH_3 compared to H_2.[23] Among these, vanadium is noteworthy, as it plays a vital role in the nitrogenase enzyme, responsible for replenishing bioavailable ammonia from atmospheric dinitrogen.[29] Vanadium carbide, oxynitrides and phosphides have been extensively reported as electrocatalysts for the NRR mostly under neutral pH conditions,[7,24,30,31] but vanadium oxides have been relatively less explored in this regard, despite the surmise that the NRR actually operates at O-supported vanadium Lewis acidic sites.[27,28] DFT calculations indicate that N_2 activation is energetically favoured on O-supported V centres by ~18 kcal mol^{-1} compared to that on N-supported V centres.[32] A survey of the literature disclosed that the coordination environment and oxophilicity of the metal are important in modulating the performance of electrocatalysts, as these properties affect the binding of N atoms and N_2 molecules on the substrate and the stability of the intermediates culminating in the release of NH_3.[33] Catalysts with electron-deficient centres were reported to be beneficial for NRR performance enhancement.[27] On the other hand, carbon-based nanomaterials have garnered widespread attention for electrocatalytic applications owing to their mechanical stability, superior electrical conductivity and enhanced surface areas. Doping of heteroatoms on the carbon surface creates defect sites and a redistribution of electrons to regulate the electron transfer and alters the sorption of reactants, intermediates and products on the catalyst surface. N-doped carbon substrates have been reported to facilitate N_2 adsorption and N≡N cleavage, though they show very mild electrocatalytic NRR activity.[13,34] Though there are a couple of reports on the utility of vanadium oxide and N-doped carbon individually for the electrocatalytic NRR, their combined efficacy is yet to be explored for the NRR, to the best of our understanding.

Motivated by the above discussions, we present vanadium dioxide encased in an N-doped carbon support (**VO_2@CN**) as an electrocatalyst for the NRR. A multidimensional structure due to a combination of vanadium dioxide and N-doped carbon is expected to improve the exposure of active sites and increase electrical conductivity, which might facilitate electrochemical nitrogen fixation. Considering the advantage of reactive Lewis acidic oxo-vanadium centres for efficient N_2 adsorption and the stability of vanadium oxides over broad potential and pH ranges,[35] we have explored **VO_2@CN** as an electrocatalyst for the NRR under acidic and neutral electrolyte conditions. Facilitated by the effectual N_2 adsorption, and stabilization of vanadium in multiple oxidation states to modulate multiple electron-transfer steps, **VO_2@CN** exhibits a high NH_3 yield of 0.31 and 0.52 μmol h^{-1} mg_{cat}^{-1} and a maximum FE of 67.9% and 61.9% at −0.1 V *vs*. RHE, under neutral and acidic conditions, respectively. The complexities of the NRR could be minimized by the detection of the intermediates formed during the course of the reaction under both electrolyte conditions using *in situ* ATR-IR studies. This in turn paves the way for a better understanding of the reaction kinetics on the **VO_2@CN** surface.

Results and discussion

Synthesis and structural characterization

A simple solution-processing route followed by carbonization (Fig. 1a) was employed to synthesize **VO_2@CN**. First, vanadium pentoxide was dissolved in 3 M HNO_3 to form $VO_2(NO_3)$ species. The acidic solution of oxo-vanadium species was thoroughly mixed with a solution of melamine in methanol. The resultant precipitate was evaporated to dryness, where the oxo-vanadium ions were trapped by the melamine moieties, resulting in the formation of $VO_2(NO_3)$@melamine (referred to as **VO_2@mel** hereafter). The reaction proceeded by carbonization under an inert atmosphere at 600 °C to yield the **VO_2@CN** material. NH_3 liberated during the thermolysis of melamine at elevated temperatures acted as a reducing agent to convert V^{+5} in **VO_2@mel** to V^{+4} in **VO_2@CN**.[36] The coordination of dinitrogen to transition metal centres is usually facilitated by a lower oxidation state of the metal.[37] In the case

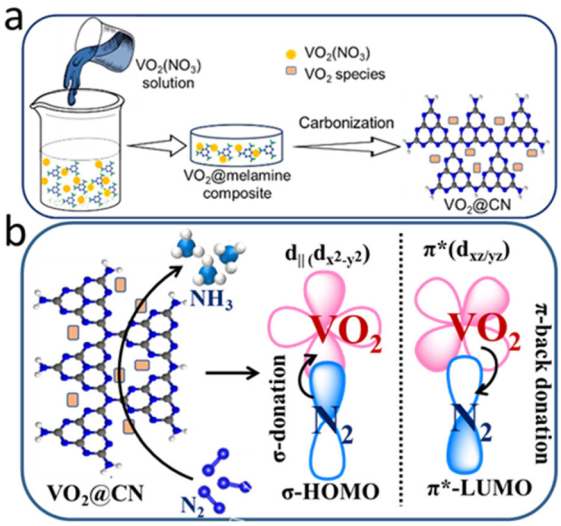

Fig. 1 (a) Schematic representation of the synthesis of **VO_2@CN**; (b) orbital interaction between N_2 and the VO_2 centre of the catalyst, responsible for N_2 reduction to NH_3 (NRR).

of vanadium, V^{+5} is the most stable oxidation state, while the lower oxidation states are often sensitive to air and moisture. The N-doped carbon matrix in **VO_2@CN** not only aids in imparting stability to VO_2, but it is expected to facilitate the NRR. It is envisaged that the VO_2 component of the catalyst would bring about σ-donation and counter π-back donation interactions between the highest occupied molecular orbitals (HOMOs) and lowest unoccupied molecular orbitals (LUMOs) of the catalyst active site and N_2, as schematically illustrated in Fig. 1b. This interaction would help weaken the N≡N bond strength, activating the molecule towards a successful reduction reaction. It is to be noted that V^{+5} in the precursor **VO_2@mel** cannot favour π-back donation to weaken the N≡N bond. The PXRD analysis of the as-synthesized material shows distinct peaks corresponding to vanadium dioxide, which can be assigned to the monoclinic phase of VO_2 (JCPDS file no. 01-082-0661, space group $P2_{1/c}$) (Fig. 2).[38] The presence of melamine in acidic solution prevents the fast aggregation of VO_6 octahedra to favour the exclusive formation of the stable monoclinic VO_2 (M) phase. The absence of any other phases in the as-prepared sample ascertains the purity of the VO_2 (M) phase. The presence of N-doped carbon was supported by the appearance of a broad signal at ~2θ = 23° corresponding to the 002 plane. The FTIR spectrum of **VO_2@CN** (Fig. S2†) shows the presence of a sharp band at ~435 cm^{-1} characteristic of the long-range stretching vibrations of the V–O–V bridge and at ~684 cm^{-1} indicative of the packing of VO_6 octahedra, respectively.[39] The breathing mode of triazine can be observed from a peak at ~813 cm^{-1}. In addition, the incorporation of nitrogen into the carbon framework can be identified from an FTIR signal at ~1372 cm^{-1}.[40] Broad bands at ~3200 cm^{-1} are attributable to N–H stretching and hydrogen bonding in the **VO_2@CN** sample. Raman spectroscopy was performed under the excitation wavelength of 532 nm, which revealed three peaks at 1373 cm^{-1}, 1598 cm^{-1} and 2760 cm^{-1} corresponding to the D, G and 2D bands of N-doped carbon, respectively (Fig. S3†). The calculated I_D/I_G value of 1.13 indicated the introduction of nitrogen atoms into the carbon framework resulting in significant lattice distortion.[41] TGA measurements reveal multiple weight loss phases until ~450 °C indicative of the release of adhered water molecules and interlayer water molecules, respectively, followed by the decomposition of N-doped carbon layers beyond 600 °C (Fig. S4†).[42]

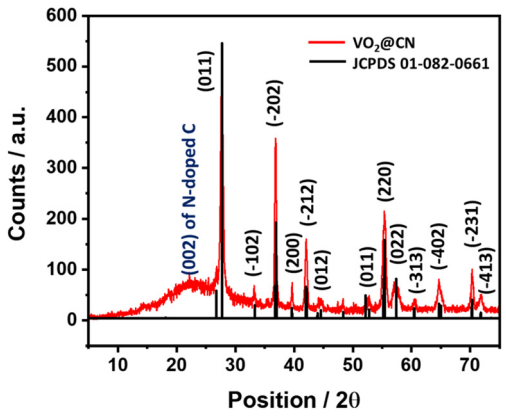

Fig. 2 PXRD pattern of the as-synthesized **VO_2@CN** indicating the presence of VO_2 (M) and N-doped carbon.

The microenvironment of **VO_2@CN** and its precursor **VO_2@mel** was investigated from X-ray photoelectron spectroscopy (XPS) measurements (Fig. 3a–c, ES1†). As shown in Fig. 3a, the V $2p_{3/2}$ spectrum exhibited a V^{+4} feature at binding energy 515.9 eV, and a feature at 516.8 eV indicative of the surface oxidation of vanadium to the V^{+5} state, which has been reported for vanadium oxide samples.[43] A V $2p_{1/2}$ signal was observed at binding energy 523.8 eV. The O 1s spectrum revealed the presence of V–O bonds at 529.45 eV and V^{+4}–O^{-2} bonds at 530.14 eV (Fig. 3b). Another peak at 531.77 eV indicated OH^- on the VO_2 surface.[28] The N 1s spectrum of **VO_2@CN** depicted the presence of three peaks at binding energies of 398.7 eV, 399.6 eV and 401.0 eV, which can be assigned to pyridinic N, pyrrolic N and graphitic N, respectively (Fig. 3c).[27] In contrast, the analysis of the valence state of the precursor **VO_2@mel** (Fig. S1†) revealed the prominent presence of the V^{+5} state in the V 2p XPS results (binding energy 516.9 eV for V $2p_{1/2}$). The N 1s XP spectrum of **VO_2@mel** revealed the presence of three peaks ascribed to the ring C=N of melamine (398.5 eV), exocyclic –NH_2 of melamine (399.6 eV) and nitrate counter anion (406.0 eV), attributed to the presence of $VO_2(NO_3)$ in **VO_2@mel**.[28]

The scanning electron microscopy (SEM) images of **VO_2@CN** revealed vanadium dioxide particles as rectangular block-shaped structures with a length of ~500 nm amidst larger crumpled sheets of N-doped carbon, which did not show any significant alteration from the morphology of pristine N-doped carbon materials (Fig. 3d and S5†). The larger size of the VO_2 rods could be attributed to the favourable grain growth of nanorods at elevated temperatures.[38] The presence and uniform distribution of the constituent elements V, O, C and N was attested from the EDX and elemental mapping analysis (Fig. S6†). The transmission electron micrographs (TEM) of **VO_2@CN** supported the presence of VO_2 blocks encased in crumpled N-doped carbon layers (Fig. 3e). HRTEM confirmed the presence of VO_2 encapsulated in N-doped carbon from the lattice fringes corresponding to a *d*-spacing value of 0.32 nm (Fig. 3f) indicative of the (011) plane of VO_2 (M). The SAED pattern depicts the polycrystalline nature of the **VO_2@CN** sample supporting the observation of N-doped carbon-encased VO_2 blocks (Fig. S7†).

Electrochemical NRR performance of VO_2@CN

Vanadium in various forms has been a popular candidate having abilities to reduce dinitrogen electrochemically.[7,43] Mostly, vanadium nitrides are investigated for the NRR, but the involvement of lattice nitrogen and the unstable metal centre have prompted researchers to explore the oxy-nitride class of materials, where the oxygen-supported vanadium centres were proved to be energetically more favourable towards N_2 scission as compared to the nitrogen supported

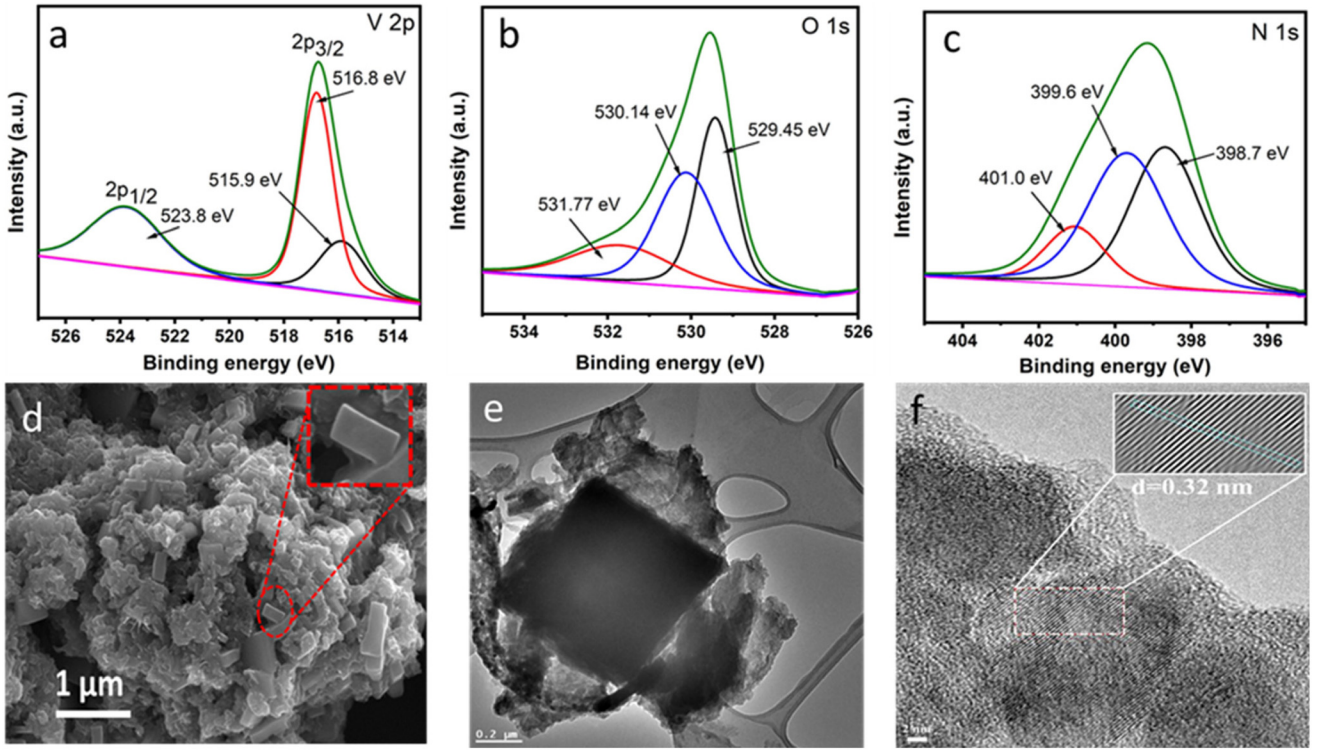

Fig. 3 XPS spectra of **VO_2@CN**: (a) V 2p, (b) O 1s and (c) N 1s. (d) FESEM image of **VO_2@CN** indicating the presence of blocks of VO_2 encapsulated in crumpled N-doped C layers. TEM and HRTEM images of **VO_2@CN** are presented as (e) and (f), respectively.

ones.[44] Investigation of V_2O_5 nanodots as an electrocatalyst for the NRR afforded a faradaic efficiency (FE) of 28.7%, attributable to the presence of oxygen vacancies that participated in the electron transfer to the V^{+5} state, to effectively generate V^{+4}, thus underlining the importance of the V^{+4} species in electrocatalytic NRR.[28] Moreover, vanadium-based systems were mostly found effective for the NRR at neutral pH, and have rarely been explored under acidic conditions in order to suppress the competing HER. Since the challenging part in the NRR is the bond polarization of N_2 leading to its first protonation and subsequent conversion to ammonia, it forms the motivation for the catalyst (**VO_2@CN**) synthesis in this work. All the potentials reported in this work were calibrated with respect to a reversible hydrogen electrode (RHE) following eqn (1) (ESI†). It was shown by Biswas *et al.* that the choice of the electrolyte is important as different catalysts respond differently in the presence of the ionic environment of the electrolyte (effect of the counter ions), and it crucially determines the nitrogen reduction performance of the catalyst.[45,46] The ions from the electrolyte form a Stern layer across the electrode that mediates the adsorption of N_2 and repels H^+ from the electrode.[47] It should be noted that the rationale behind avoiding the basic electrolyte is attributed to sample instability in the medium. Thus, in this study both acidic (0.1 M HCl) and neutral (0.1 M Na_2SO_4) electrolytes were explored, and a comparative study was accomplished. Before any electrochemical tests, the electrolyte solutions were degassed with Ar followed by N_2 purging after passing the N_2 feed gas through base and acid traps since contamination is unavoidable in the NRR and this calls for all precautionary measures to achieve reliable data. The electrochemical cell set-up used in this study is shown in Fig. S8.† As shown in Fig. S9,† the trap solutions were subjected to colorimetric tests for the detection of any dissolved NO_x or NH_4^+ that would have been present in the feed gas. The UV-visible spectra for the N_2-trapped solutions were overlaid with those of the bare ones, which indicated that there were negligible gaseous nitrogenous impurities in the feed gas itself.

Thereafter, an elaborate study with chronoamperometry (CA) at different potentials was carried out in both the electrolytes for 1 h each (Fig. S10a and c†). The post-electrochemistry UV-visible studies with the electrolytes stained with colouring agents (indophenol blue method), depicted a maximum absorbance corresponding to the indophenol dye formed out of the produced ammonia at −0.1 V *vs.* RHE (Fig. S10b and d†). The material **VO_2@CN** displayed a better ammonia yield rate (calculated using eqn (2), ESI†) in 0.1 M HCl as shown in the bar plot in Fig. 4a, while the FE (calculated using eqn (2), ESI†) in Fig. 4b was better in the case of Na_2SO_4. In fact, in the case of HCl, the FE showed a drastic reduction as we approached more closely towards a negative potential, owing to enhanced hydrogen evolution reaction (HER) kinetics. The acidic electrolyte with abundant proton sources helped to protonate the produced ammonia, which remained dissolved in the electrolyte

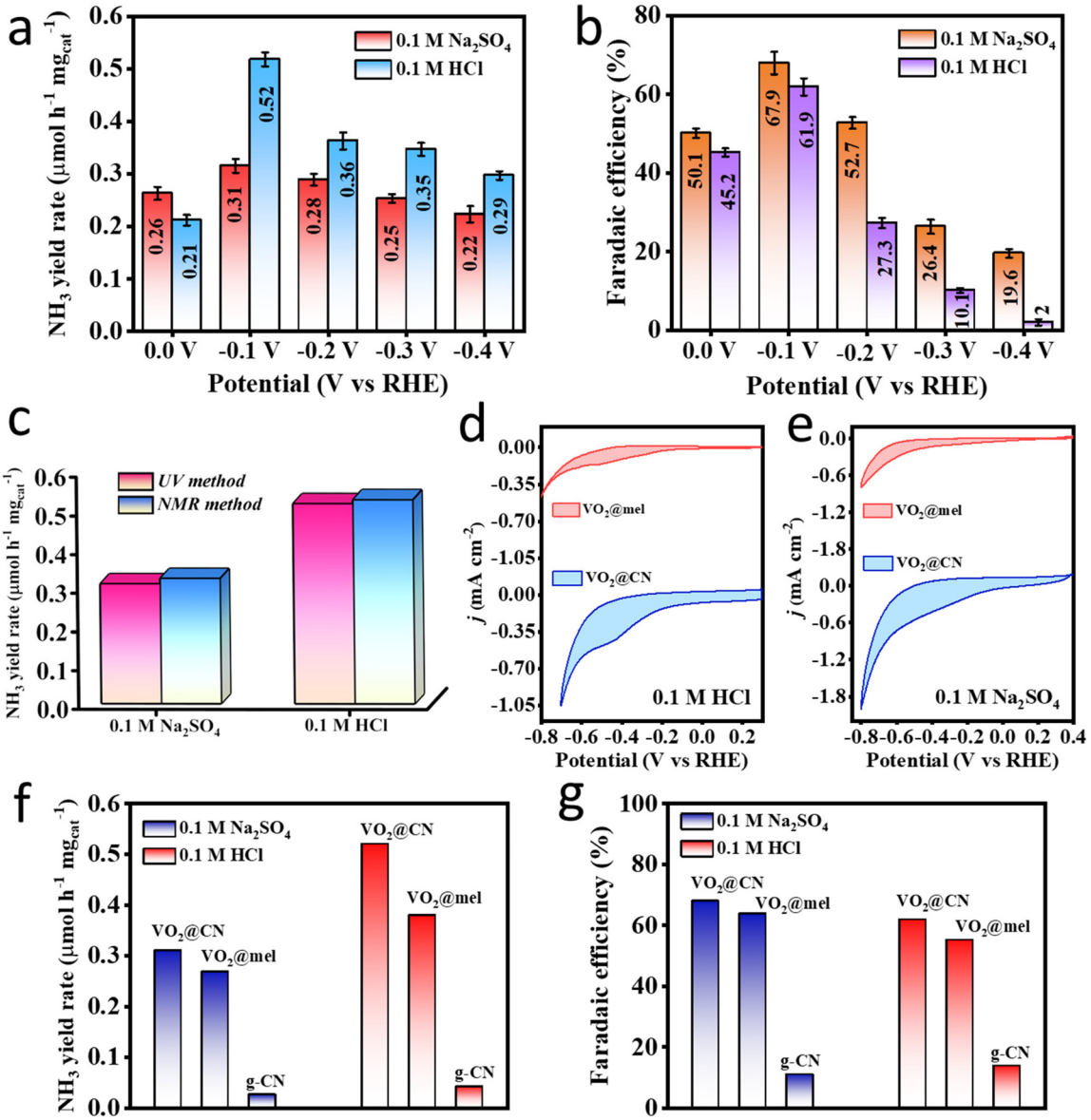

Fig. 4 NRR performance comparison of the **VO_2@CN** catalyst in both 0.1 M Na_2SO_4 and 0.1 M HCl electrolytes. (a and b) NH_3 yield rate and FE of the catalyst over the wide-ranging potential window from 0.0 V to −0.4 V *vs.* RHE in the presence of continuous N_2 purging; (c) quantitative analyses of NRR performance of **VO_2@CN** using UV-visible and NMR methods; CV curves of **VO_2@CN** and **VO_2@mel** samples in (d) 0.1 M HCl and (e) 0.1 M Na_2SO_4 showing an enhancement in the current density upon graphitization of melamine due to increased conductivity; (f) NH_3 yield rate and (g) FE comparison of **VO_2@CN** with control samples like **VO_2@mel** and g-CN in both acidic and neutral electrolyte media. The error bars represent the standard deviation values for three different data-sets.

in the form of NH_4^+ and ensured no loss as NH_3 gas. However, at the same time, it also induced proton adsorption on the catalyst surface since the HER is a less energy-intensive process than the NRR, which caused the catalyst to incur a sacrificial FE over the entire potential range. With a maximum FE of 67.9% and 61.9% in Na_2SO_4 and HCl respectively at −0.1 V *vs.* RHE, the material was also proved to be selective towards ammonia production as there was no interference from side-product (hydrazine) formation (Fig. S10e and f†). This could be justified with respect to a very recent report by Huang *et al.* that experimentally and theoretically suggested that the NRR on V active sites could energetically prefer a distal pathway negating the chances of the formation of hydrazine, rightly corroborating our experimental results.[48] Thus, the NRR on our active material of **VO_2@CN** was kinetically facilitated yielding 0.31 and 0.52 μmol h^{-1} mg_{cat}^{-1} of NH_3 in Na_2SO_4 and HCl, respectively. The concentrations of ammonia in all cases were calculated using the standard calibration curves and the corresponding linear regression plot in the relevant acidic or neutral electrolytes (Fig. S11 and S12†). The interference from hydrazine formation was interpreted from the standard calibration and corresponding linear-fitted curves in both the elec-

trolytes, as shown in Fig. S13.† It is noteworthy to mention that the bare Ti foil (pre-cleaned and used instantaneously in order to avoid any surface oxidation layer) showed an FE of 3.24% and 9.5% in 0.1 M Na_2SO_4 and 0.1 M HCl, respectively, as shown in the bar diagram in Fig. S14,† which indicated that there was only a slight interference of the substrate towards the NRR and it was the right choice to purposely use Ti foil as a substrate as it helped to elevate material performance.

Since the nuclear magnetic resonance (NMR) method provides more accurate quantification, it was adopted to verify the NH_3 yield rate and FE in acidic and neutral electrolytes. The details are provided in the ESI.† It is worth noting from Fig. S15† that, in both media, while there was no peak under Ar-purged conditions, a triplet appeared in the presence of N_2 resembling $^{14}NH_4^+$ (coupling constant value of 52 Hz calculated using eqn (3) in the ESI†). Thereafter, a quantitative calculation using maleic acid as the standard (eqn (4) from the ESI†) revealed similar NH_3 yield rates from both UV-visible and NMR methods, as shown in Fig. 4c, that justify the reliability of the experimental data. However, it is true that without control experiments it is not rational to claim the superiority of the catalyst. Thus, we took into consideration two control samples, *i.e.* the precursor **VO_2@mel**, and g-CN for the study as the former would show the importance of a conducting carbon framework to anchor the active centres while the latter would justify the role of VO_2 active sites of the catalyst for the NRR (detailed NRR studies and UV-visible data are shown in Fig. S16†). As expected, the CV curves at 10 mV s^{-1} in Fig. 4d and e in 0.1 M HCl and 0.1 M Na_2SO_4 respectively show an enhancement in the areal current as well as cathodic current density for **VO_2@CN** as compared to **VO_2@mel** signifying the enhancement of the electron conductivity due to the graphitization of melamine to the CN framework. However, the NH_3 yield rate and FE for **VO_2@mel**, although sound enough, were lower when compared to that of **VO_2@CN** (Fig. 4f and g) because V was primarily in the V^{+5} oxidation state, which reduced the π-back donation to the LUMO of the N_2 molecule; thus the cleavage of N≡N bond was relatively less. So, a long-term CA experiment would result in a loss of active sites from the catalyst surface. In contrast to this, the NRR performance of the g-CN sample was very low, being devoid of VO_2 units (Fig. 4f and g). This clearly manifested the role of VO_2 as the NRR active site with the simultaneous importance of the conjugated carbon–nitride framework in the pronounced electrocatalytic performance of our final material **VO_2@CN** towards the NRR.

Mechanistic investigation and identification of NRR intermediates by *in situ* ATR-FTIR studies. The electrochemical NRR is a complex multi-step process, where the N_2 activation and reduction depend largely on the nature of the catalyst active site. The orbital interactions accompanying σ-donation and π-back donation between the active site and N_2 serve as the primary steps of the NRR initiating N_2 adsorption and activation. V is known to catalyze the NRR and, in this work, the V-center of the VO_2 unit in **VO_2@CN** is considered the active unit where the presence of adjacent O atoms could reorganize the electron occupancy of the molecular orbital levels of metallic VO_2 further assisted by the N-doped carbon support.[49] Thus, the $d_{||}$ and π* orbitals of VO_2 could likely participate in the respective bonding–anti-bonding orbital interactions with the σ-highest occupied molecular orbital (HOMO) and π*-lowest unoccupied molecular orbital (LUMO) of N_2, as schematically shown in Fig. 5a. This interaction is followed by the N≡N bond polarization and the protonation steps that produce several obscured reaction intermediates on the catalyst surface. Out of these, the stable intermediates are detected in the *in situ* ATR-FTIR spectra including those attributed to peaks at 1307 and 1460 cm^{-1} observed in both electrolytes *i.e.*, 0.1 M Na_2SO_4 and 0.1 M HCl (Fig. 5b and c), resembling H–N–H rocking and N–H bending, respectively.[50] It is important to note that the peak corresponding to N–N stretching could be attributed to a stable H_2N–NH_2 intermediate on the catalyst surface and the corresponding peak appeared to be slightly red-shifted in HCl (1139 cm^{-1}) than in the neutral electrolyte (1143 cm^{-1}) suggesting the better extent of N–N bond polarization in the acidic medium and faster reaction kinetics. This also supported our claim for product (NH_3) selectivity of the material as we did not obtain any trace of N_2H_4 from the UV-visible spectra. Furthermore, the abundance of protons in the acidic electrolyte activated the polarized N_2 molecules giving a better yield rate for NH_3 production with a comparatively faster kinetics. However, it is also noteworthy that the FTIR spectra in the acidic electrolyte were much more noisy owing to the simultaneous evolution of H_2 (HER) on the catalyst surface along with the NRR, which although produced NRR intermediates and products, the current thus obtained contributed to the HER resulting in a sacrificial FE for the NRR in HCl rather than in Na_2SO_4. Thus, it is interesting to note that keeping all the electrochemical conditions the same, different electrolytes create different local electronic/ionic environments at the catalyst–electrolyte interface and variedly influence the NRR at the active site.

NRR stability studies and post-stability material characterization. Since the **VO_2@CN** catalyst shows a significant NRR performance in both acidic and neutral media, it was obvious to note a distinct deviation in the CV curves for the material under both Ar- and N_2-purged electrolyte conditions (Fig. S17†). For the sake of negating the possibilities of false positive results, several control CA experiments, like (a) **VO_2@CN** in the presence of Ar at −0.1 V and (b) **VO_2@CN** in N_2 at the open circuit potential (OCP), were conducted (Fig. S18a–d†). Although, at the OCP, there was negligible production of ammonia, under an Ar atmosphere, there was a nominal yield rate and FE for NH_3 wherein, the lattice N could partially partake in the electrocatalytic process following the Mars van Krevelen mechanism.[32] However, this was trivial when compared to that obtained in the presence of N_2 in both electrolytes. Furthermore, the sustainability of the catalyst was investigated with stability studies, where in both electrolytes after 12 h of continuous CA experiment (Fig. 6a–d), the catalyst showed a drop in ammonia production and NRR performance (Fig. 6c). This could be ascribed to (a) material loss from the

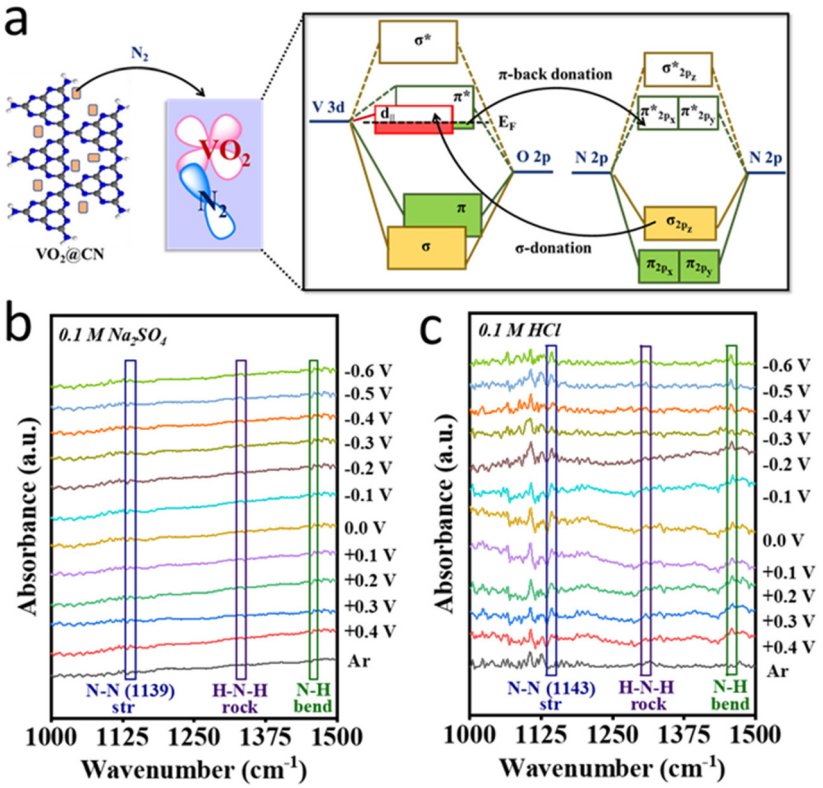

Fig. 5 (a) Orbital interaction between the VO_2 part of **VO_2@CN** and N_2 in terms of a molecular orbital diagram; unprocessed *in situ* ATR-FTIR spectra of the catalyst at different working potentials under N_2- and Ar-purged conditions in (b) 0.1 M Na_2SO_4 and (c) 0.1 M HCl, respectively.

electrode surface or (b) leaching of V-active sites from the catalyst upon prolonged exposure to the electrolyte under a constant potential of −0.1 V with the conditions being more prominent in the case of HCl (FE reduces from 61.9% to 45.7% after 12 h) than Na_2SO_4 (FE decreases from 67.9% to 55.2% after 12 h). These data are in accordance with several reports on vanadium-based systems for the NRR.[51,52] However, they did not suggest any effect on the morphology of the post-stability **VO_2@CN** sample as is evident from the FESEM and TEM images shown in Fig. S19a and b† along with the uniform presence of all the constituent elements like C, N, O and V on the electrode surface, as shown from the elemental mapping in Fig. S19c and d.† In fact, the XRD spectrum in Fig. S20a† displayed combined features of both **VO_2@CN** and the underlying carbon cloth (used as a substrate for stability studies). To distinguish the peaks, the spectrum was zoomed and compared with that of the bare carbon cloth (CC) and fresh **VO_2@CN** samples, wherein all the peaks appeared to have been retained in the post-electrolysis sample (Fig. S20b†) suggesting the persistent lattice structure of the material. However, there was some change in the chemical bonding of the material upon prolonged electrolysis, as demonstrated from the XPS studies.

XPS studies were conducted for **VO_2@CN** samples after the electrochemical NRR stability experiments under HCl and Na_2SO_4, respectively, and compared with the pristine sample (Fig. 3a–c and 6d–f). The XPS data reveal minor alterations in the surface structure of the **VO_2@CN** catalyst after electrochemical NRR. Under both pH conditions, the V 2p spectrum shifts towards a slightly lower binding energy, indicative of the removal of the surface oxidized V^{+5} (BE 516.4 eV in post-NRR samples *vs.* 516.8 eV in pristine) species that was observed in the pristine sample (Fig. 3a). In all cases, the pronounced V $2p_{3/2}$ maxima around the binding energy of 516 eV indicated V^{+4} as the major species (Fig. 6d).[53] However, there is a reduction in the atomic percentage of vanadium in the post-NRR samples, which can be ascribed to the leaching of VO_2 species in solution during the NRR. There is a significant increment in the post-NRR intensity of the O 1s signals around the binding energies of ~531 eV and 532.4 eV ascribed to the prominence of oxide and adsorbed hydroxyl species, respectively (Fig. 6e). Unlike the case of the oxynitride species reported in the literature, the shift of the N 1s signal to lower binding energies (*i.e.* towards 396.5 eV)[32] and any significant depletion in the N content of N-doped C were not observed in our case (Fig. 6f). There was no evidence of N-incorporation in **VO_2@CN** from the N_2-saturated electrolyte under NRR conditions, consistent with the literature reports.[54] It should be mentioned here that the changes in the core level spectra of V 2p, O 1s and N 1s are induced by cathodic polarizations in HCl and Na_2SO_4 electrolytes, and not due to exposure under ambient conditions.[55] The greater ease in protonation of the

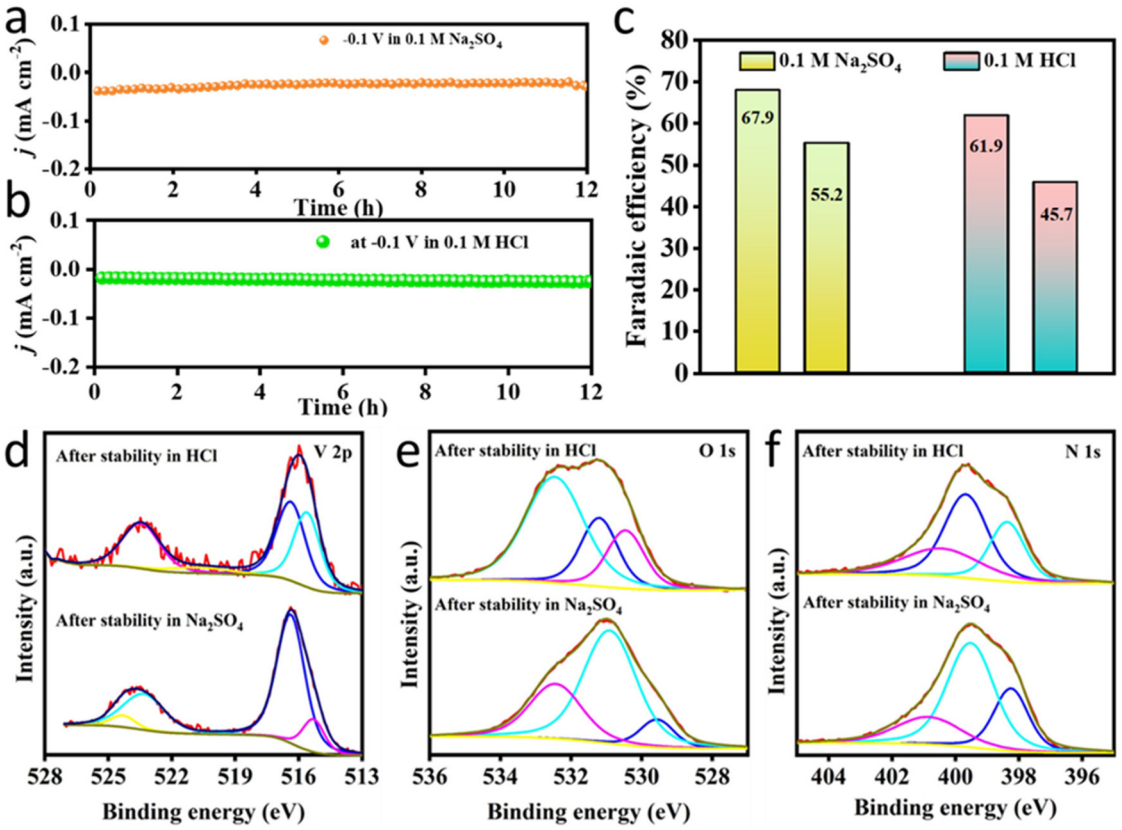

Fig. 6 (a and b) CA response of **VO_2@CN** during the NRR at −0.1 V *vs.* RHE in 0.1 M Na_2SO_4 and 0.1 M HCl, respectively, for a continuous 12 h period; (c) FE comparison of the catalyst after 1 and 12 h of NRR studies in both electrolytes; post-NRR XPS profiles for (d) V 2p, (e) O 1s and (f) N 1s, respectively, under HCl and Na_2SO_4 electrolyte conditions.

surface-bound N_2 on vanadium oxide suggests that the increased acidity of the vanadium active site bound to the electronegative oxygen atoms and encapsulated in N-doped carbon stabilized the intermediates of the NRR and facilitated dinitrogen cleavage. This trend has been mentioned for other metals with high oxophilicity, including NbO_2, which exhibited a high FE for the NRR.[56] Thus, it can be concluded that there are several factors that rule the choice of electrolyte in the NRR. It is not a good practice to go with the catalyst performance for a 1 h potential-dependent study as the electrolyte might have a poisoning effect on the catalyst active site by either blocking or causing leaching of the active centre. This fact has relevance with respect to this study as it reveals that although the yield of NH_3 was better in the acidic electrolyte, Na_2SO_4 stood out as a better contender in terms of FE and the stability study of the **VO_2@CN** catalyst.

Experimental section

Synthesis of VO_2@CN

4 g of melamine was added to a 250 mL round bottomed flask containing 50 mL of methanol. The solution was then stirred at room temperature for about 30 minutes. 300 mg of vanadium pentoxide dissolved in 20 mL of 3 M nitric acid was added to the solution containing melamine under continuous stirring. The reaction mixture was stirred for another hour under ambient conditions. The precipitate was evaporated to dryness.

The obtained VO_2@melamine (**VO_2@mel**) was transferred into an alumina boat placed inside a tubular furnace and heated to 600 °C under continuous nitrogen flow for 3 h to obtain a black powder named **VO_2@CN**.

Conclusions

In our quest to identify an inexpensive, Earth-abundant material as a universal-pH electrocatalyst for the NRR, we explored vanadium oxide encased in N-doped carbon, an Earth-abundant transition metal oxide that is synthesizable in bulk quantities. The data reported here designate **VO_2@CN** as an efficient and selective electrocatalyst for nitrogen fixation with a high NH_3 yield of 0.31 and 0.52 μmol h^{-1} mg_{cat}^{-1} and a maximum FE of 67.9% and 61.9% at −0.1 V *vs.* RHE, under neutral and acidic conditions, respectively, without any observable incorporation of nitrogen into the vanadium oxide lattice. Furthermore, *in situ* ATR-FTIR studies at different potentials under N_2 and Ar revealed the obscured reaction intermediates of the NRR and justified the differential activity

trend of **VO_2@CN** under both electrolyte conditions, owing to the possible impact of the competitive HER. In addition, the selectivity of the material was ascertained from the absence of side-products like hydrazine and suppression of the competing hydrogen evolution reaction. Our results demonstrate the competence of vanadium oxide on N-doped carbon as an electrocatalyst for the NRR under variable pH conditions, and substantiates oxophilicity as an important factor in designing electrocatalysts.

Author contributions

AC: methodology, formal analysis, data curation (synthesis and characterization), and writing – original draft, AB: methodology, formal analysis, data curation (electrocatalytic NRR), and writing – original draft. SP: data curation (characterization) and writing – review and editing. RSD: funding acquisition, supervision (AB), and writing – review and editing. JM: funding acquisition, supervision (AC and SP), writing – original draft, and writing – review and editing.

Conflicts of interest

There are no conflicts to declare.

Acknowledgements

JM acknowledges DST SERB (SPG/2021/004430) and RSD acknowledges DST SERB (CRG/2020/005683) and BRE-BRNS (58/14/19/2023-BRNS) for financial assistance. Analytical support from AESD&CIF, CSMCRI and INST is gratefully acknowledged. CSMCRI PRIS No. 149/2023.

References

1 R. F. Service, *Science*, 2014, **345**, 610–610.
2 W. Qiu, X. Y. Xie, J. Qiu, W. H. Fang, R. Liang, X. Ren, X. Ji, G. Cui, A. M. Asiri, G. Cui, B. Tang and X. Sun, *Nat. Commun.*, 2018, **9**, 3485.
3 M. H. Hasan, T. M. I. Mahlia, M. Mofijur, I. M. R. Fattah, F. Handayani, H. C. Ong and A. S. Silitonga, *Energies*, 2021, **14**, 3732.
4 B. H. R. Suryanto, H. Du, D. Wang, J. Chen, A. N. Simonov and D. R. Macfarlane, *Nat. Catal.*, 2019, **2**, 290–296.
5 J. G. Chen, R. M. Crooks, L. C. Seefeldt, K. L. Bren, R. M. Bullock, M. Y. Darensbourg, P. L. Holland, B. Hoffman, M. J. Janik, A. K. Jones, M. G. Kanatzidis, P. King, K. M. Lancaster, S. V. Lymar, P. Pfromm, W. F. Schneider and R. R. Schrock, *Science*, 2018, **360**, eaar6611.
6 G.-F. Chen, S. Ren, L. Zhang, H. Cheng, Y. Luo, K. Zhu, L.-X. Ding and H. Wang, *Small Methods*, 2019, **3**, 1800337.
7 J. Pan, H. A. Hansen and T. Vegge, *J. Mater. Chem. A*, 2020, **8**, 24098.
8 H. Hirakawa, M. Hashimoto, Y. Shiraishi and T. Hirai, *J. Am. Chem. Soc.*, 2017, **139**, 10929–10936.
9 W. Ye, M. Arif, X. Fang, M. A. Mushtaq, X. Chen and D. Yan, *ACS Appl. Mater. Interfaces*, 2019, **11**, 28809–28817.
10 A. Good, *Science*, 2018, **359**, 869–870.
11 M. Yang, T. Wei, J. He, Q. Liu, L. Feng, H. Li, J. Luo and X. Liu, *Nano Res.*, 2024, **17**, 1209–1216.
12 G. Zhang, G. Wang, Y. Wan, X. Liu and K. Chu, *ACS Nano*, 2023, **17**, 21328–21336.
13 Y. Liu, Y. Su, X. Quan, X. Fan, S. Chen, H. Yu, H. Zhao, Y. Zhang and J. Zhao, *ACS Catal.*, 2018, **8**, 1186–1191.
14 X. Han, C. S. Gerke, S. Banerjee, M. Zubair, J. Jiang, N. M. Bedford, E. M. Miller and V. S. Thoi, *ACS Energy Lett.*, 2020, **5**, 3237–3243.
15 U. K. Ghorai, S. Paul, B. Ghorai, A. Adaldar, S. Kapse, R. Thapa, A. Nagendra and A. Gain, *ACS Nano*, 2021, **15**, 5230–5239.
16 S. L. Foster, S. I. P. Bakovic, R. D. Duda, S. Maheshwari, R. D. Milton, S. D. Minteer, M. J. Janik, J. N. Renner and L. F. Greenlee, *Nat. Catal.*, 2018, **1**, 490–500.
17 M. Arif, G. Yasin, L. Luo, W. Ye, M. A. Mushtaq, X. Fang, X. Xiang, S. Ji and D. Yan, *Appl. Catal., B*, 2020, **265**, 118559.
18 S. Chen, G. Qi, R. Yin, Q. Liu, L. Feng, X. Feng, G. Hu, J. Luo, X. Liu and W. Liu, *Nanoscale*, 2023, **15**, 19577–19585.
19 K. Chen, J. Xiang, Y. Guo, X. Liu, X. Li and K. Chu, *Nano Lett.*, 2024, **24**, 541–548.
20 J. Zhao, L. Zhang, X. Y. Xie, X. Li, Y. Ma, Q. Liu, W. H. Fang, X. Shi, G. Cui and X. Sun, *J. Mater. Chem. A*, 2018, **6**, 24031–24035.
21 H. Tao, C. Choi, L. X. Ding, Z. Jiang, Z. Han, M. Jia, Q. Fan, Y. Gao, H. Wang, A. W. Robertson, S. Hong, Y. Jung, S. Liu and Z. Sun, *Chem*, 2019, **5**, 204–214.
22 M. Nazemia, S. R. Panikkanvalappila and M. A. El-Sayed, *Nano Energy*, 2018, **49**, 316–323.
23 E. Skulason, T. Bligaard, S. Gudmundsdottir, F. Studt, J. Rossmeisl, F. Abild-Pedersen, T. Vegge, H. Jonsson and J. K. Norskov, *Phys. Chem. Chem. Phys.*, 2012, **14**, 1235–1245.
24 P. Chukwunenye, A. Ganesan, M. Gharaee, K. Balogun, F. Anwar, Q. Adesope, T. R. Cundari, F. D'Souza and J. A. Kelber, *J. Mater. Chem. A*, 2022, **10**, 21401.
25 R. Manjunatha, A. Karajić, V. Goldstein and A. Schechter, *ACS Appl. Mater. Interfaces*, 2019, **11**, 7981–7989.
26 Z. Qiao, D. Johnson and A. Djire, *Cell Rep.*, 2021, **2**, 100438.
27 L. Wang, Y. Liu, H. Wang, T. Yang, Y. Luo, S. Lee, M. G. Kim, T. T. T. Nga, C.-L. Dong and H. Lee, *ACS Nano*, 2023, **17**, 7406–7416.
28 W. Li, Y. Ye, M. Jin, S. Zhang, C. Lin, C. Sun, Y. Zhang, G. Wang, C. Liang and H. Zhang, *Chem. Eng. J.*, 2023, **451**, 139494.
29 Y. Hu, C. C. Lee and M. W. Ribbe, *Dalton Trans.*, 2012, **41**, 1118–1127.

30 C. Zhang, D. Wang, Y. Wan, R. Lv, S. Li, B. Li, X. Zou and S. Yang, *Mater. Today*, 2020, **40**, 18–25.
31 X. Li, L. Li, X. Ren, D. Wu, Y. Zhang, H. Ma, X. Sun, B. Du, Q. Wei and B. Li, *Nano Res.*, 2020, **13**, 2967–2972.
32 A. Osonkie, A. Ganesan, P. Chukwunenye, F. Anwar, K. Balogun, M. Gharaee, I. Rashed, T. R. Cundari, F. D'Souza and J. A. Kelber, *ACS Appl. Mater. Interfaces*, 2022, **14**, 531–542.
33 K. Balogun, A. Ganesan, P. Chukwunenye, M. Gharaee, Q. Adesope, S. Nemšák, P. S. Bagus, T. R. Cundari, F. D'Souza and J. A. Kelber, *J. Phys.: Condens. Matter*, 2023, **35**, 333002.
34 L.-H. Zhang, F. Yu and N. R. Shiju, *ACS Sustainable Chem. Eng.*, 2021, **9**, 7687–7703.
35 M. Privman and T. Hepel, *J. Electroanal. Chem.*, 1995, **382**, 137–144.
36 A. Wen, Z. Cai, Y. Zhang and H. Liu, *RSC Adv.*, 2022, **12**, 13093–13103.
37 D. Sellamnn, *Angew. Chem., Int. Ed. Engl.*, 1974, **13**, 639–649.
38 J. Hou, Z. Wang, Z. Ding, Z. Zhang and J. Zhang, *Sol. Energy Mater. Sol. Cells*, 2018, **176**, 142–149.
39 S. Liang, Q. Shi, H. Zhu, B. Peng and W. Huang, *ACS Omega*, 2016, **1**, 1139–1148.
40 A. Misra, P. K. Tyagi, M. K. Singh and D. S. Misra, *Diamond Relat. Mater.*, 2006, **15**, 385–388.
41 K. Gong, F. Du, Z. Xia, M. Durstock and L. Dai, *Science*, 2009, **323**, 760–764.
42 S.-Z. Huang, Y. Cai, J. Jin, Y. Li, X.-F. Zheng, H.-E. Wang, M. Wu, L.-H. Chen and B.-L. Su, *J. Mater. Chem. A*, 2014, **2**, 14099–14108.
43 X. Yang, J. Nash, J. Anibal, M. Dunwell, S. Kattel, E. Stavitski, K. Attenkofer, J. G. Chen, Y. Yan and B. Xu, *J. Am. Chem. Soc.*, 2018, **140**, 13387–13391.
44 F. D'Souza, A. Ganesan, A. Osonkie, P. Chukwunenye, I. Rashed, F. Anwar, M. Gharee, K. Balogun, T. R. Cundari and J. A. Kelber, ECS Meeting Abstracts, 2022, **MA2022-01** (45), 1893–1893.
45 A. Biswas, S. Kapse, R. Thapa and R. S. Dey, *Nano-Micro Lett.*, 2022, **14**, 214.
46 A. Biswas, S. Kapse, B. Ghosh, R. Thapa and R. S. Dey, *Proc. Natl. Acad. Sci. U. S. A.*, 2022, **119**, e2204638119.
47 S. C. Jesudass, S. Surendran, J. Y. Kim, T.-Y. An, G. Janani, T.-H. Kim, J. K. Kim and U. Sim, *Electrochem. Energy Rev.*, 2023, **6**, 27.
48 W. Huang, L. Y. Peng, J. Zhang, C. Liu, G. Song, J. H. Su, W. H. Fang, G. Cui and S. Hu, *J. Am. Chem. Soc.*, 2023, **145**, 811–821.
49 N. B. Aetukuri, A. X. Gray, M. Drouard, M. Cossale, L. Gao, A. H. Reid, R. Kukreja, H. Ohldag, C. A. Jenkins, E. Arenholz, K. P. Roche, H. A. Dürr, M. G. Samant and S. S. P. Parkin, *Nat. Phys.*, 2013, **9**, 661–666.
50 S. Bhardwaj, S. K. Das, A. Biswas, S. Kapse, R. Thapa and R. S. Dey, *Chem. Sci.*, 2023, **14**, 8936–8945.
51 R. Manjunatha, A. Karajić, H. Teller, K. Nicoara and A. Schechter, *ChemCatChem*, 2020, **12**, 438–443.
52 Y. Abghoui and E. Skúlason, *J. Phys. Chem. C*, 2017, **121**, 6141–6151.
53 M. C. Biesinger, L. W. M. Lau, A. R. Gerson and R. S. C. Smart, *Appl. Surf. Sci.*, 2010, **257**, 887–898.
54 A. Ganesan, A. Osonkie, P. Chukwunenye, I. Rashed, T. R. Cundari, F. D'Souza and J. A. Kelber, *J. Electrochem. Soc.*, 2021, **168**, 026504.
55 A. Glaser, S. Surnev, F. P. Netzer, N. Fateh, G. A. Fontalvo and C. Mitterer, *Surf. Sci.*, 2007, **601**, 1153–1159.
56 L. Huang, J. Wu, P. Han, A. M. Al-Enizi, T. M. Almutairi, L. Zhang and G. Zheng, *Small Methods*, 2019, **3**, 1800386.